Nanoscale

PAPER

View Article Online
View Journal | View Issue

Cite this: *Nanoscale*, 2025, **17**, 9974

Probing the interactions in graphene oxide/MoS_2 and reduced graphene oxide/MoS_2 nanoarchitectures using multimodal scanning probe microscopy†

Amanda F. Pereira,[a] Ariane Schmidt,[a] Bernardo R. A. Neves,[b] Camilla K. B. Q. M. de Oliveira[c] and Aldo J. G. Zarbin *[a]

Scanning probe microscopy (SPM) encompasses a versatile set of characterization techniques that reveal different properties and characteristics of materials. Herein, we demonstrate the potential of combining different SPM modes to understand the interactions (and their properties) between the components in two-dimensional/two-dimensional nanoarchitected thin films: graphene oxide (GO)/molybdenum disulfide (MoS_2) and reduced graphene oxide (rGO)/MoS_2. The films were prepared through the liquid–liquid interfacial route and analyzed by atomic force microscopy in topographic and phase contrast images, Kelvin probe force microscopy, lateral force microscopy and peak force microscopy. It was shown that the presence of oxygenated surface groups, the occurrence of structural defects and the surface electrical potential significantly affect the morphology and properties of the films. Due to their effective electrostatic interaction, the very small MoS_2 flakes are uniformly distributed over the rGO flakes, whereas in an opposite way, they tend to agglomerate in the GO sheets. As a result, the GO/MoS_2 film exhibits Young's modulus of 30 GPa, which is lower than that of the film containing neat GO (78 GPa), due to the increase in both deformation (2.6 nm) and adhesion (7.2 nN). Otherwise, the stiffness increases from 15 GPa to 25 GPa from neat rGO to the rGO/MoS_2 nanocomposite, in which it was observed that the presence of MoS_2 increases friction and promotes n-type doping. Based on the different SPM modes, it was possible to correlate the structural and morphological characteristics with some mechanical and electrical properties of bi-component thin films, and probe the specific interactions between the components.

Received 23rd January 2025,
Accepted 26th February 2025

DOI: 10.1039/d5nr00341e

rsc.li/nanoscale

1. Introduction

Two-dimensional (2D) materials such as graphene oxide (GO), reduced graphene oxide (rGO), and molybdenum disulfide (MoS_2) are widely studied due to their superior performance in applications in different fields such as battery technology,[1–3] electronics,[4–6] optoelectronics,[7,8] sensing[9–11] and catalysts.[12–14] Although GO and rGO have some less efficient properties in comparison to pristine graphene, the presence of functional groups in these materials enables their functionalization, which allows the tailored design of materials for applications that are not possible with pristine graphene. Another approach for modifying the properties of GO and rGO is preparing nanocomposites with other materials, such as MoS_2, a low-cost and abundant 2D semiconductor material with a tunable bandgap. This combination leads to synergistic properties, broadening the scope of potential applications. For instance, Liu *et al.* reported the fabrication of an MoS_2/graphene nanocomposite for use as an anode in lithium batteries, in which the high conductivity of graphene and the ability of MoS_2 to provide more active intercalation sites and to reduce the diffusion energy barrier for Li^+ ions offer enhanced performance.[15] Similarly, Li *et al.* developed a material composed of rGO and MoS_2 that exhibited high electrocatalytic activity for the hydrogen evolution reaction when compared to catalysts containing only MoS_2.[16]

There are several examples highlighting the great potential of 2D/2D nanocomposites in various devices. However, a thorough understanding of the interactions between the components is crucial to fully exploit the properties of the materials, which can be achieved through detailed studies using advanced characterization techniques. Scanning probe

[a]*Department of Chemistry, Federal University of Paraná, Curitiba, PR 19081, Brazil. E-mail: aldozarbin@ufpr.br*
[b]*Department of Physics, ICEx, Federal University of Minas Gerais, Belo Horizonte, MG 30123-970, Brazil*
[c]*Department of Physics, Federal University of Paraná, Curitiba, PR 19081, Brazil*
† Electronic supplementary information (ESI) available. See DOI: https://doi.org/10.1039/d5nr00341e

microscopy (SPM) is a non-destructive technique that provides insights into the physical and chemical properties of materials.[17–19] SPM encompasses various methods, including phase contrast microscopy, Kelvin probe force microscopy (KPFM), lateral force microscopy (LFM), and PeakForce quantitative nanomechanical mapping (PeakForce-QNM®). These techniques are essential for analyzing the properties of materials at the nanoscale, offering valuable information on their structural, mechanical, and electrical characteristics.

Numerous studies have employed SPM to investigate the properties of 2D materials. For example, Lavini *et al.* used phase contrast imaging to explore energy dissipation in epitaxial graphene, focusing on how graphene layers respond to an oscillating probe and the different energy dissipation processes affecting the phase contrast of the probe.[20] In another study, Luo *et al.* examined the interaction between GO and transition metal carbides (MXenes) using SPM to measure force curves, revealing that the adhesive force at the heterostructure interface is influenced by charge density distribution linked to oxygenated functional groups of GO.[21] Meanwhile, Kim *et al.* studied the surface properties of functionalized graphene using LFM, uncovering the intrinsic properties of the material and enabling advances in exfoliation and surface manipulation techniques.[22] Additionally, Palma *et al.* developed a method to analyze uniformly strained monolayers of MoS_2 using KPFM,[23] an effective approach for assessing non-uniform deformation and piezoelectric properties in various 2D materials. However, the large majority of the data reported in this subject deal with the characterization of individual sheets or a set of sheets of different compositions interacting with each other but also isolated, representing several examples of so-called van der Waals structures. Very few data have been collected from these materials processed as thin films, and therefore ready for real technological applications.

One major challenge in scaling up 2D materials lies in their processing methods, which includes thin film technology. Common techniques such as spin coating, dip coating, and chemical vapor deposition are often unsuitable for forming nanocomposite thin films due to issues such as solvent incompatibility or the requirement of high temperatures, which can degrade the materials.[24–26] Our research group has focused on improving the processing of these materials into thin films through the so-called liquid–liquid interfacial route (LLIR).[27] This method relies on the self-organization of materials at the interface between two immiscible liquids, allowing the resulting film to be transferred onto a solid surface, which simplifies the whole series of steps to prepare, process and transfer complex and multicomponent thin films. Some of us have recently demonstrated the potentiality of the LLIR in preparing thin films of MoS_2/GO and MoS_2/rGO with different nanoarchitectures, obtaining improved electrochemical performances when compared to their isolated components.[28] Herein, we present a comprehensive investigation using different SPM modes to characterize the thin films of these 2D/2D materials and explore the properties arising from the interactions between MoS_2 and GO or MoS_2 and rGO. To the best of our knowledge, this is the first report on the combined use of this whole set of SPM techniques to characterize a bi-component material that has been directly processed as a thin film.

2. Experimental

2.1. Materials

Graphite (Graflake 99580 from Nacional de Grafite, Brazil), $NaNO_3$ (Vetec), $KMnO_4$ (Synth), H_2O_2 (Neon), $NaBH_4$ (Sigma-Aldrich), HCl 37% (Impex), $(NH_4)_6Mo_7O_{24}{\cdot}4H_2O$ (Vetec), $(NH_4)_2S$ aqueous solution 20% (Vetec), H_2SO_4 98% (Anidrol), acetonitrile gradient grade for liquid chromatography 99.9% LiChrosolv (Merck), and toluene 99% (Neon) were used as received. All the solutions were prepared using ultrapure water. The Si and Si/SiO_2 substrates were washed sequentially with water and neutral detergent, ultrapure water, and isopropyl alcohol to remove any type of contaminant from their surface.

2.2. Synthesis of GO, rGO and MoS_2

GO and rGO were synthesized from graphite oxide using the modified Hummers' method, as previously reported.[29,30] MoS_2 was chemically synthesized according to a chemical route previously reported by our group.[31] The detailed synthetic procedure regarding the synthesis of the precursors can be found in the ESI.†

2.3. Synthesis of the GO/MoS_2 thin film

In a 50 mL round-bottom flask containing 6 mL of MoS_2 dispersion in acetonitrile (0.23 mg mL^{-1}), 20 mL of an aqueous dispersion of GO (0.02 mg mL^{-1}) and 20 mL of toluene were added under stirring at 2500 rpm for 12 h.[28] After this period, a thin film was observed at the liquid–liquid interface. Both the solvents (water and toluene) were replaced by pure water and toluene 3 times. After that, the entire system (toluene/film/water) was transferred to a flask containing the solid substrate, and the film was transferred to the substrate by lifting it across the interface.

2.4. Synthesis of the rGO/MoS_2 thin film

rGO (30 μg mL^{-1}) was dispersed in 20 mL of toluene in an ultrasound bath for 3 hours. The dispersion was added to a 50 mL round-bottom flask containing 6 mL of MoS_2 dispersion (0.23 mg mL^{-1}) in acetonitrile and 20 mL of ultrapure water. After 3 hours of stirring at 2500 rpm, a homogeneous film was formed at the water–toluene interface, which was washed by exchanging both the aqueous phase and the organic phase 3 times with ultrapure water and toluene, respectively. The transference of the film to the substrates was done exactly as described before.

2.5. Characterization

The films at the liquid/liquid interface were transferred to Si/SiO_2 substrates in order to be analyzed by SPM using two

approaches: (i) a direct transfer of the entire film, resulting in a continuous film with the same nanoarchitecture as that prepared at the liquid/liquid interface (and all the samples prepared in this manner will be referred to here as "film"); (ii) the self-organized film at the liquid/liquid interface was destroyed, dispersed in an appropriate solvent and a drop of the dispersion was transferred to the substrate using an eye dropper, aiming to obtain a dispersed material (the samples prepared this way will be referred to here as "dispersed film").[27,32] The samples were characterized by phase contrast microscopy, using Shimadzu SPM 9700 equipment with an NCHR-20 PointProbe aluminum-coated silicon probe on the detector side from NanoWorld with a nominal resonance frequency of 320 kHz and a spring constant of 42 N m^{-1}. The same equipment was used for Kelvin probe force microscopy (KPFM) analysis. The substrates with the samples were adhered to the microscope sample holder with double-sided carbon tape. Electrostatic patterns were obtained using a Si probe coated with Pt/Ir acquired from Nanoworld with a spring constant of 2.8 N m^{-1} and a nominal resonance frequency of 75 kHz. A clean Si/SiO_2 substrate was used for probe calibration. The SPM model XE70 from Park Systems was used in contact mode for friction analysis by lateral force microscopy (LFM). The probe used was the XSC11/Hard/Al BS model coated with diamond-like carbon (DLC) obtained from MikroMasch with a spring constant of 0.2 N m^{-1} and a nominal frequency of 15 kHz. A Nanoscope IV MultiMode SPM from Veeco Instruments was used to obtain the images indicating the deformation, adhesion and elastic modulus with the force curves of the samples recorded using the Bruker PeakForce-QNM® mode. An NSC 35/Al BS probe from MikroMasch was used for this analysis with a spring constant (k) of 16 N m^{-1} and a nominal resonance frequency of 300 kHz. The probe was calibrated using the absolute method, which does not require a standard sample with a known modulus; however, it is necessary to measure the tip radius and spring constant. Additionally, the Sader method was employed to determine values of k.[33] The force applied to obtain the results was 30 nN.

3. Results and discussion

Fig. 1a–c shows the AFM topographic images of the neat control samples of GO, rGO and MoS_2, demonstrating that all films are homogeneous and continuous, covering the entire substrate by an interconnected arrangement of individual sheets. Fig. S1 (ESI†) shows the images of the dispersed films, in which geometrical areas of the isolated sheets were observed as being approximately 0.3 μm^2 for GO, 0.7 μm^2 for rGO and 0.005 μm^2 for MoS_2. It is important to note that the MoS_2 sample used in this work is much smaller in size than the GO and rGO samples. Furthermore, these samples range from monolayer to few-layer thicknesses, with the latter exceeding 10 nm in thickness, as can be seen in the histograms presented in Fig. S1.†

Phase contrast images of the films (Fig. 1d–f) reveal an abrupt change in the phase of the tip as it passes through the edges of each individual sheet. This phenomenon can be seen in the three control films and cannot be seen in the phase contrast images of the individual sheets obtained from the dispersed films, presented in Fig. S1b, f and j,† which indicates that it is a collective effect arising from the film structure, due to the edge/edge contact between the individual sheets to generate the continuous films.

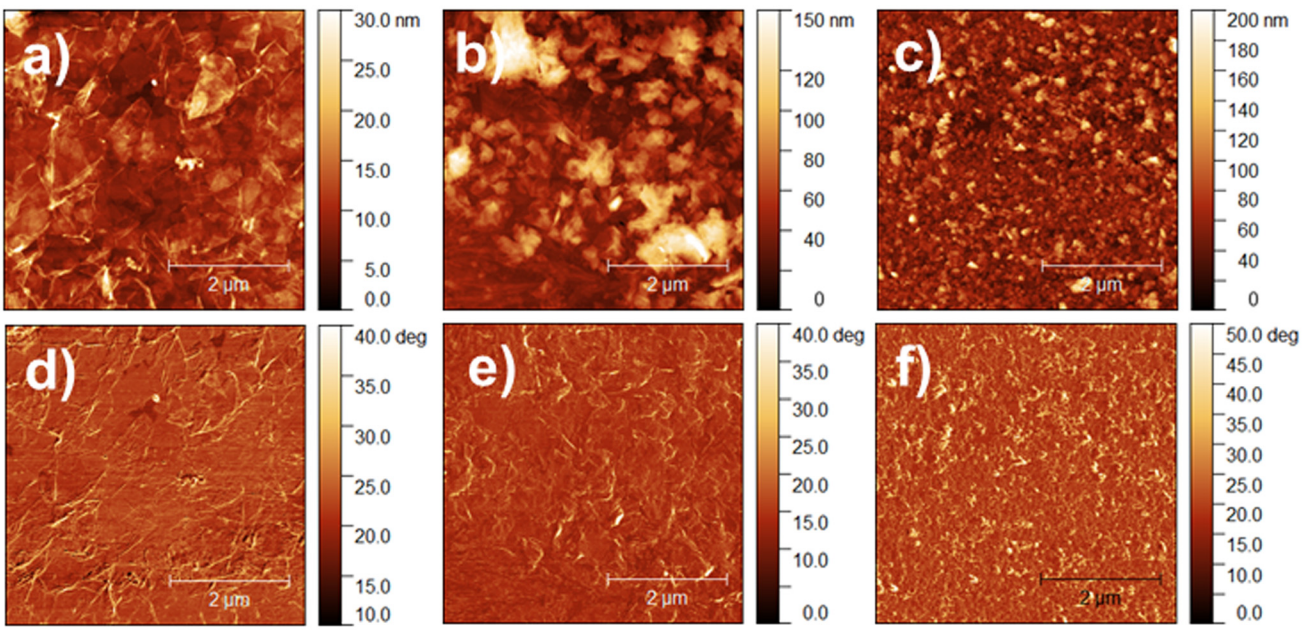

Fig. 1 (a–c) AFM topographic and (d–f) phase-contrast images of (a and d) GO, (b and e) rGO and (c and f) MoS_2 films. AFM topographic and phase-contrast images were obtained simultaneously and correspond to the same region.

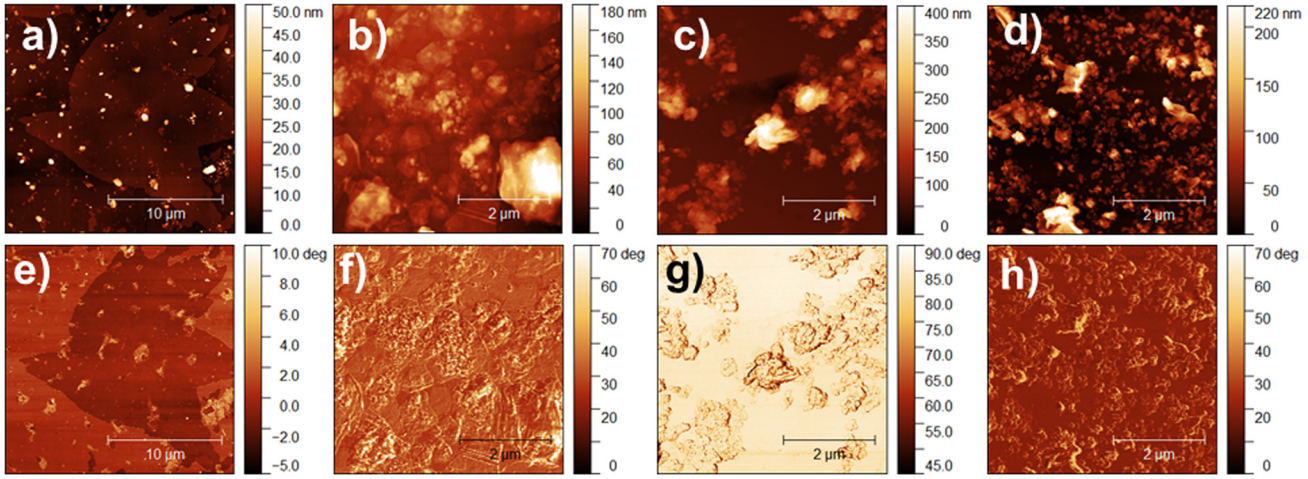

Fig. 2 (a–d) AFM topographic and (e–h) phase-contrast images of (a, b, e and f) GO/MoS_2 and (c, d, g and h) rGO/MoS_2 where (a, c, e and g) show dispersed films and (b, d, f and h) show continuous films. The topographic and phase-contrast images were obtained simultaneously and correspond to the same region.

The AFM images of the nanocomposites (Fig. 2) reveal a significant difference between the samples. It is clear preferential agglomeration of the MoS_2 flakes occurs at specific points on the GO sheets (Fig. 2b), in contrast to the well-dispersed distribution of MoS_2 over the entire area of the rGO film (Fig. 2d). This kind of distribution can be seen more clearly in the dispersed film images, shown in Fig. 2a, c, e and g. Once the samples have been prepared in the same way, and keeping the ratio between the components fixed, the morphology of the films presented in Fig. 2 suggests an improved interaction between MoS_2 and rGO and a less-favourable interaction between MoS_2 and GO, leading to more uniform distribution of the components in the rGO/MoS_2 film compared to that in the GO/MoS_2 film. The specific experimental procedure in which the samples were prepared can explain these differences: previous research indicates that MoS_2 flakes are electrostatically stabilized in an acetonitrile/water dispersion by negative charges,[31] exactly as observed for GO that has the carboxylic groups at the edges deprotonated under the experimental conditions during the film deposition (pH = 4.2),[34] leading to repulsion between the two materials. The electrostatic repulsion results in the domains of agglomerated MoS_2 observed in the AFM images. Otherwise, the hydrophobic nature of rGO facilitates a π-ion-like interaction between rGO and MoS_2, maximizing the interactions. Furthermore, it is observed that the phase contrast is more pronounced between GO and MoS_2 (Fig. 2f) than between rGO and MoS_2 (Fig. 2h), where the tip phase experiences a large change as it passes through the region with MoS_2 agglomeration.

The KPFM data of the films are shown in Fig. 3 (Fig. S2† for the dispersed films). The electrostatic potential maps with

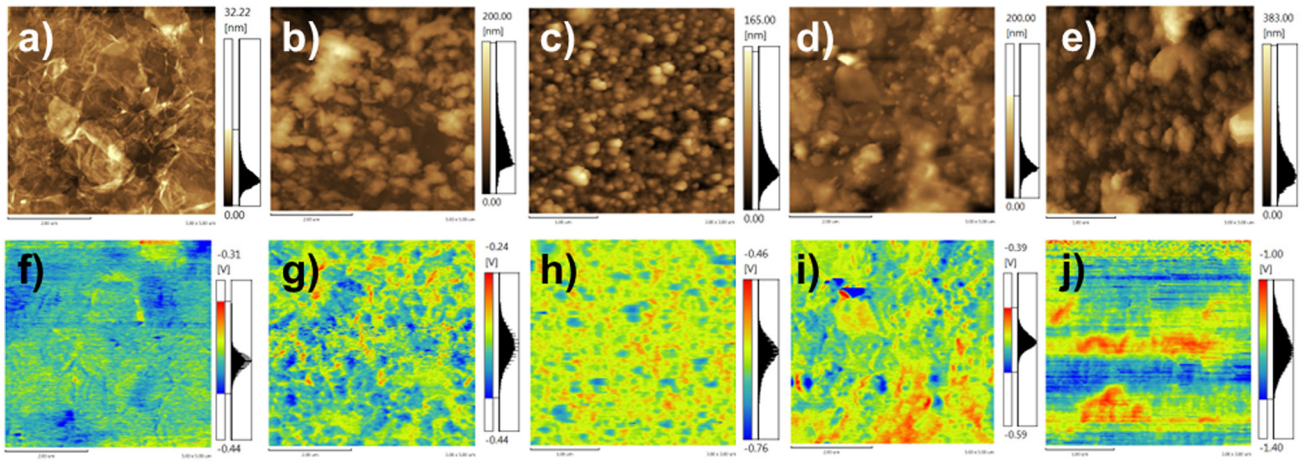

Fig. 3 (a–e) Topographic AFM images and their respective (f–j) KPFM images of (a and f) GO with ΔV = −0.39 V, (b and g) rGO with ΔV = −0.36 V, (c and h) MoS_2 with ΔV = −0.60 V, (d and i) GO/MoS_2 with ΔV = −0.50 V, and (e and j) rGO/MoS_2 with ΔV = −1.23 V. Films deposited on an Si/SiO_2 substrate. Topographic and KPFM images were obtained simultaneously and correspond to the same region.

their corresponding topographic images reveal nuanced insights into the characteristics of the films. The surface potential difference was taken from the average of the histogram located on the right side of each KPFM image. First of all, it is clear that the electric potential is not uniform over the entire surface of the films, and second, it is different between the samples. Notably, neat GO, rGO and MoS_2 exhibit small surface potential differences of approximately −0.39 V for the GO film, −0.36 V for the rGO film and −0.60 V for MoS_2, due to the presence of structural defects and/or the concentration of oxygenated functional groups, as previously discussed.

The following equation was used to calculate the work function (Φ) of the films:

$$V_{CPD} = (\Phi_{film} - \Phi_{tip})/e \quad (1)$$

where V_{CPD} is the contact potential difference between the tip and the film, Φ_{film} and Φ_{tip} are the work function (WF) values of the film and the tip (Pt/Ir-coated Si cantilever with a WF of 5.5 eV)[35] and e is the electron charge. The work functions of GO, rGO and MoS_2 films are 5.1 eV, 5.2 eV and 4.9 eV, respectively. The rGO and MoS_2 films exhibited a WF similar to those reported in the literature.[36,37] However, the GO film displayed a higher WF than previously reported (around 4.4–4.6 eV).[38] Rodriguez *et al.* highlighted several factors that can be responsible for increasing the work function of GO, including: (i) the oxidation degree of GO, which generates surface dipoles; (ii) the thickness of the layers, which increases the surface potential; and (iii) the random orientation of the sheets, enhancing the edge effect. The difference between the WF of the GO film is slightly lower than that of the rGO film due to both the number of functional groups and the thickness of these materials.[37,39] Since the rGO film produced here is thicker than the GO film, the contribution of this factor added to the disorder of the sheets, which contributes to this film having a slightly higher WF than the GO film.

In respect of these concerns for the nanocomposites, the KPFM maps presented in Fig. 3 clearly indicate the differences of the interactions between MoS_2 and GO or between MoS_2 and rGO. The KPFM map of the GO/MoS_2 nanocomposite (Fig. 3d and i) clearly shows that MoS_2 has a more negative charge in relation to GO, corroborating the data discussed before related to the negative charges induced in MoS_2 flakes during exfoliation in acetonitrile.[31,40] The WF of the nanocomposite was 5.0 eV, a little bit lower than that of the neat GO film. On the other hand, MoS_2 is more positively charged compared to rGO in the rGO/MoS_2 film (Fig. 3e and j), which shows a WF = 4.3 eV, much lower than the WF values of the individual components. Similar results have been described for the interaction between isolated sheets of these materials: Li *et al.* reported an effective charge transfer between graphene and MoS_2, suggesting a weak ionic interaction between them.[41] These authors suggest that the interaction between MoS_2 and graphene leads to the induction of a positive charge in the MoS_2 flakes, while the graphene acquires a corresponding negative charge. Guo *et al.* have noted that the edge effect in MoS_2 significantly impacts its surface potential through electron redistribution.[42] These findings are in accordance with our results, and suggest that the more pronounced surface charge differences in the rGO/MoS_2 film, compared to the GO/MoS_2 one, facilitate a more uniform distribution of MoS_2 flakes across the rGO sheets, which could improve the charge transfer or a doping process and decrease the WF of the nanocomposite. More detailed KPFM images acquired from the samples prepared from the dispersion of films can be found in Fig. S2 and S3.†

Fig. 4 presents the LFM images alongside topographic representations of GO-dispersed, rGO-dispersed and MoS_2-dispersed films, outlining the variation in friction of the component in relation to the SiO_2 substrate. In the LFM images, darker regions correspond to lower friction while lighter regions indicate higher friction. The GO-dispersed film exhibits higher friction compared to the substrate (Fig. 4a and d). This is attributed to the abundance of oxygenated functional groups on the GO sheets, which enhance the resistance encountered by the probe as it moves across the sheet.[43] On the other hand, the rGO-dispersed film demonstrates significantly lower friction relative to the substrate, as expected, considering the inherent lubricating properties of rGO, a property commonly associated with graphene.[44]

In the images of the MoS_2-dispersed film (Fig. 4c and f), it is possible to notice that some flakes have different friction coefficients from each other, which can be attributed to the anisotropic nature of the MoS_2 flakes, which present a distribution of the number of stacked sheets and consequently a height difference between them (as discussed before). This phenomenon was documented by Sun *et al.*, who found that MoS_2 flakes with less than nine layers on Si/SiO_2 substrates exhibit variable friction coefficients with respect to the probe contact angle.[45] Another explanation can be attributed to the variations in the charge density between the different flakes containing different stacked layers, which can influence friction coefficients through the interaction of the probe with the charged flakes on the substrate.[46]

The LFM images of GO, rGO and MoS_2 films are shown in Fig. 5. The observed changes in the frictional properties of these films are predominantly attributed to the probe resistance encountered when sliding over obstacles of increased thickness, such as folds and wrinkles. Furthermore, the presence of residual oxygenated functional groups that were not completely eliminated after the reduction process, or structural defects that modify the interaction of the probe with the film, can also contribute to this phenomenon, as observed in phase contrast images.[47,48] LFM images of the GO film (Fig. 5d) reveal areas of reduced friction (darker regions) that were not detected in the contact mode topographic image (a detailed comparison can be seen in the magnification of the area demarcated by a dashed square in Fig. 5a and d), accentuating the decrease in friction, which has been attributed by us as being due to the presence of intercalated water. GO is expected to present pronounced hydrophilicity due to the abundance of oxygenated groups in its structure, allowing the

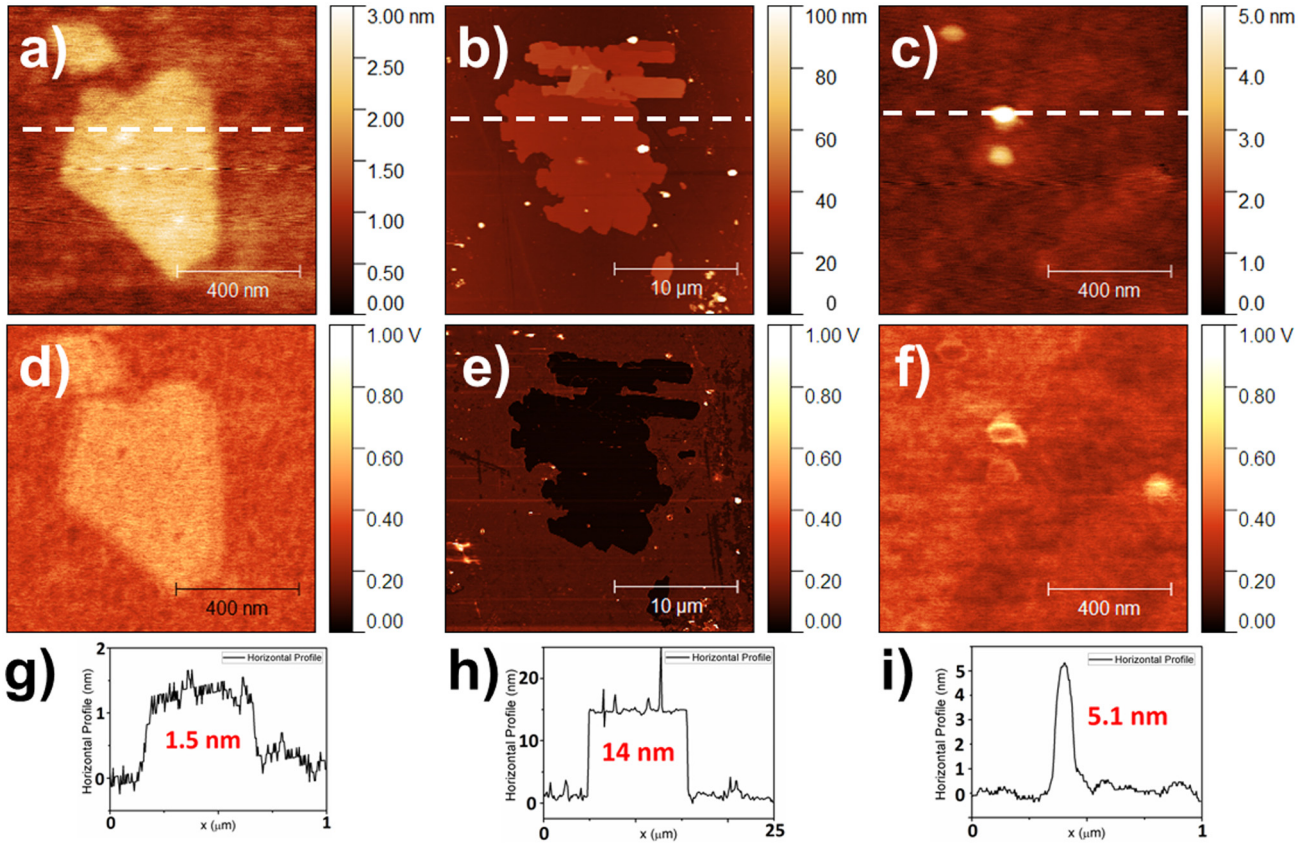

Fig. 4 (a–c) AFM topographic images, (d–f) LFM images and (g–i) their respective horizontal height profiles (along the dashed white lines in a, b and c) of (a, d and g) the GO-dispersed film with a thickness of 1.5 nm, (b, e and h) the rGO-dispersed film with a thickness of 14 nm and (c, f and i) the MoS_2-dispersed film with a thickness of 5.1 nm, deposited on Si/SiO_2 substrates. In the LFM images, darker regions indicate lower friction and lighter regions indicate higher friction. Topographic and LFM images were obtained simultaneously and correspond to the same region.

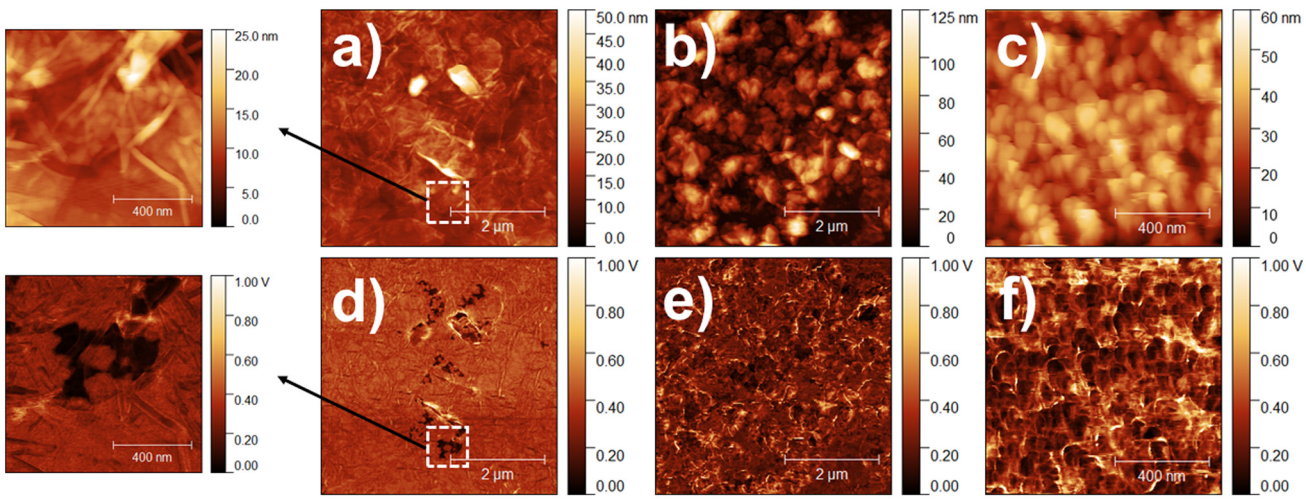

Fig. 5 (a–c) AFM topographic images and (d–f) LFM images of (a and d) GO (figures at left are the magnified images of the areas denoted by white squares in (a) and (d), showing the presence of intercalated water in the LFM mode which is not noticeable in the topographic image); (b and e) rGO and (c and f) MoS_2 films deposited on an Si/SiO_2 substrate. In the LFM images, darker regions have less friction and lighter regions have higher friction. Topographic and LFM images were obtained simultaneously and correspond to the same region.

intercalation of water between its layers and the substrate. This is strongly favored by the experimental procedure in which the films have been prepared, allowing water molecules to be trapped between GO sheets interacting to generate the film. Kim *et al.* reported that such trapped water acts like a lubricant,[49] resulting in a decrease in the friction, as observed in our sample. Furthermore, Paliy *et al.* have shown that the increased interaction between water and the substrates lead to lower static and kinetic frictional forces.[50] In essence, substrates with higher hydrophilicity are associated with reduced friction. However, such a pattern is not observed in the images of the GO-dispersed film sample, suggesting that the intercalated water originates from the film deposition process on the substrate.

The LFM images of all samples also reveal that the edges of the individual sheets exhibit higher friction (brighter areas) when compared to the basal planes of the flakes, showing again the strong edge-effect on the films, as previously discussed. This effect was not seen in the rGO film, as expected, owing to rGO having a more hydrophobic nature.

Fig. 6 and Fig. S4† present the LFM and topographic images of the nanocomposite films and dispersed films, respectively. Similar to the observed phase contrast images, LFM images of the GO/MoS_2 film present areas with different friction coefficients, due to the occurrence of different materials. In the analyzed region, the presence of an area without distinct morphology was again observed (marked with a dashed square in Fig. 6a and c), which represents a region with reduced friction (darker region), which is not detected in the topographic image, exactly as seen in the image for the neat GO film discussed before, and attributed to the intercalated water that is a result of the film deposition method. Furthermore, the MoS_2 flake agglomerations present regions of higher friction (brighter regions) than the rest of the film. The results presented indicate that the presence of MoS_2 tends to increase the friction of the nanocomposite, as observed in the literature and explained by the high polarizability of the sulfur atoms that increases the interaction of the probe with the sample.[51] In our sample, the more negatively charged MoS_2 compared to GO, which causes the MoS_2 agglomeration over the GO, is responsible for the higher friction detected in the LFM images. In the image of the rGO/MoS_2 film, MoS_2 flakes can be seen dispersed between the folded graphene sheets. The LFM image reveals areas of lower friction, correlating with the rGO sheets. Furthermore, the interaction between rGO and MoS_2 exhibited higher friction relative to the films composed solely of rGO or MoS_2, as reported by Vazirisereshk *et al.*[51]

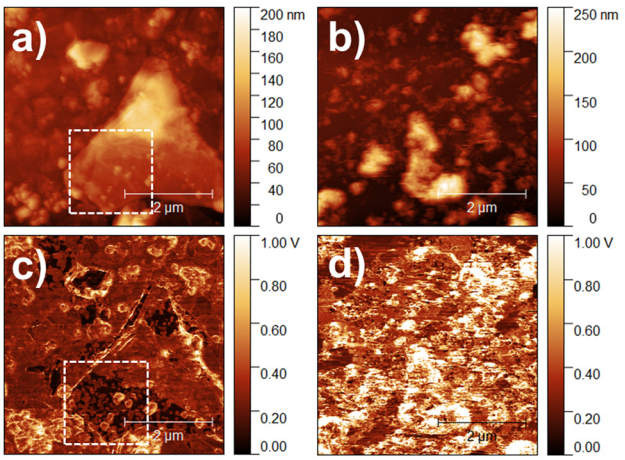

Fig. 6 (a and b) AFM topographic images and (c and d) LFM images of (a and c) GO/MoS_2 and (b and d) rGO/MoS_2 films deposited on an Si/SiO_2 substrate. In the LFM images, the darker regions are regions with less friction and the lighter regions are regions with higher friction. Topographic and LFM images were obtained simultaneously and correspond to the same region.

PeakForce-QNM® analysis facilitates the acquisition of detailed mechanical properties regarding adhesion forces, material deformation and Young's modulus.[52] Fig. 7 and 8 present the mapping of deformation, adhesion forces and Young's modulus, accompanied by topographical images of the films. Similar data collected from analysis of the dispersed films can be found in Fig. S5.† Images of GO, rGO and MoS_2 films show pronounced deformation and adhesion in their folds and edges compared to other areas of the sheets, indicating different behaviors between the borders and the basal planes of the sheets in the films, exactly as also observed in the phase-contrast and LFM images. This is a very interesting observation because the individual flakes are connected by the borders to generate the continuous film, so it can be associated with a flake–flake interaction phenomenon. These characteristics are believed to contribute to the observed reduction in Young's modulus throughout the film, compared to individual sheets. The greater deformation and adhesion are attributed to the lack of adhesion of the sheets to the substrate, leading to a wrinkling effect as the probe passes through these regions, in addition to the presence of oxygenated groups and defects at the edges of the sheet. Furthermore, structural defects, as evidenced in the rGO images (dashed square area 2 in Fig. 7), also play a role in altering these properties by decreasing the stiffness of the film; for rGO, the stiffness measured was 15 GPa. The deformation image further reveals the role of water intercalated in the GO film (dashed square area 1 in Fig. 7), which is likely a consequence of the deposition method, as previously discussed in the LFM analysis. This interaction between GO and water is essential to increase the deformation and adhesion of the film and, at the same time, reduce the Young's modulus. Medhekar *et al.* elucidated that the stiffness of GO layers is modulated by the presence of water, which induces a structural reorganization of the water molecules beneath the GO layers, culminating in an increase in the deformation and a consequent reduction in the stiffness, which was 78 GPa.[53] The MoS_2 film exhibits Young's modulus of 18 GPa, in contrast to the reported values for individual sheets between 120 and 330 GPa. The differences are directly related to the sample properties: the majority of published data were collected from CVD-grown MoS_2 corresponding to samples

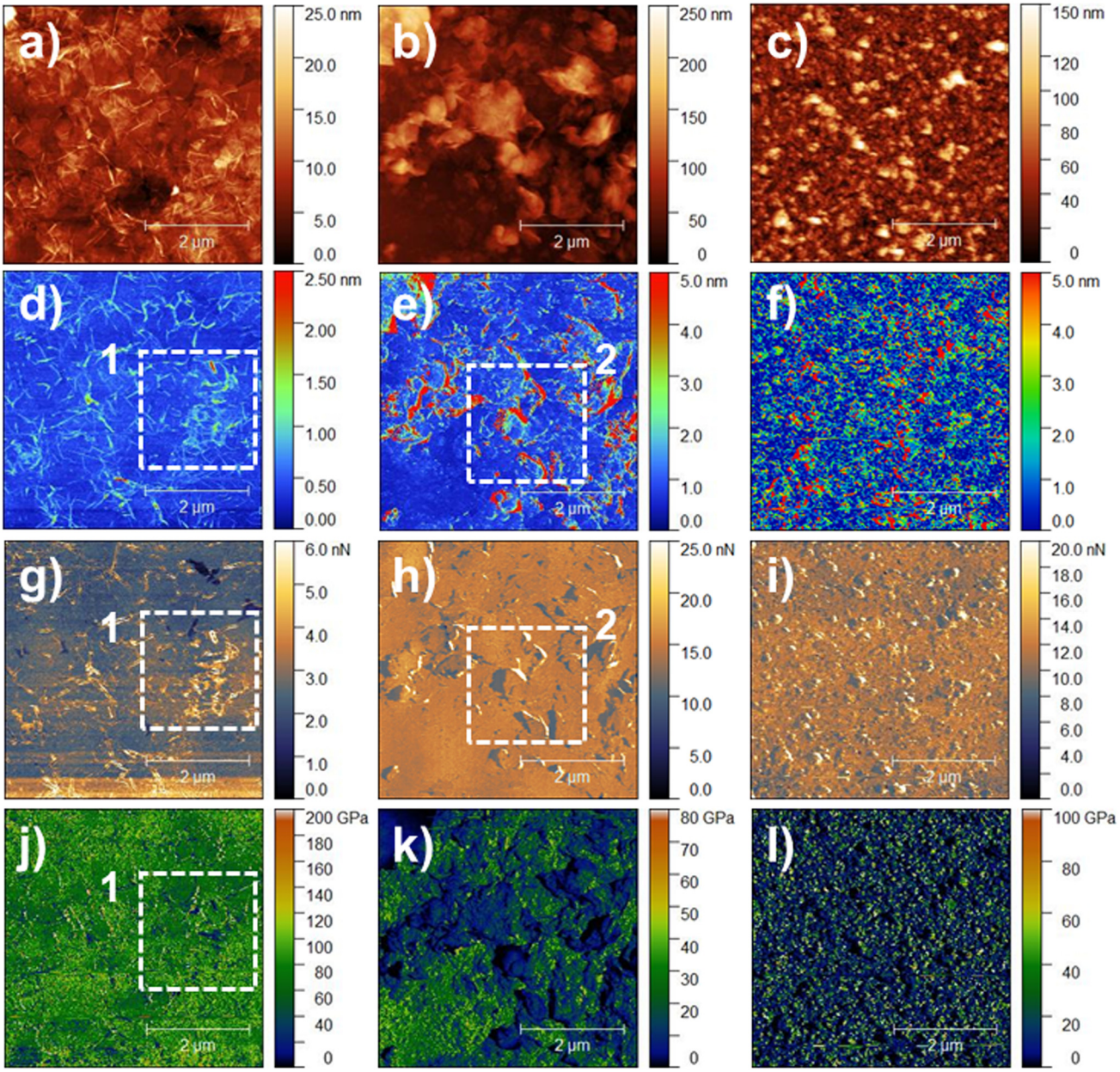

Fig. 7 (a–c) AFM topographic images, (d–f) deformation images, (g–i) adhesion force images and (j–l) Young's modulus images of (a, d, g and j) GO, (b, e, h and k) rGO and (c, f, i and l) MoS_2 films deposited on an Si/SiO_2 substrate. Topographic, deformation, adhesion force and Young's modulus images were obtained simultaneously and correspond to the same region.

with flakes of micrometric lateral dimensions,[54–57] while the MoS_2 sample employed here is characterized by its nanometric lateral dimensions, a factor that contributes to the observed reduction in material stiffness due to the increased incidence of structural defects and borders. It is also worth noting that most reported studies explored the properties of individual nanomaterial sheets with low thickness, while here we analyzed their continuous films. This processing of these materials orients their final properties, as observed and discussed in the KPFM images, where the random re-stacking of the sheets favors the edge effect, which is much more defective than the basal plane, resulting in a decrease in the stiffness of the material.

The GO/MoS_2 film images show regions exhibiting high deformation and low adhesion (dashed square area 3 in Fig. 8). These areas correspond to the MoS_2 regions and the edges or folds of the GO sheets, which support prior observations made using LFM. Such changes in mechanical properties significantly affect Young's modulus values. The resulting stiffness of the film was 30 GPa, a value that is notably lower than the 78 GPa stiffness of the GO film. However, this represents an improvement over the MoS_2 film, indicating that

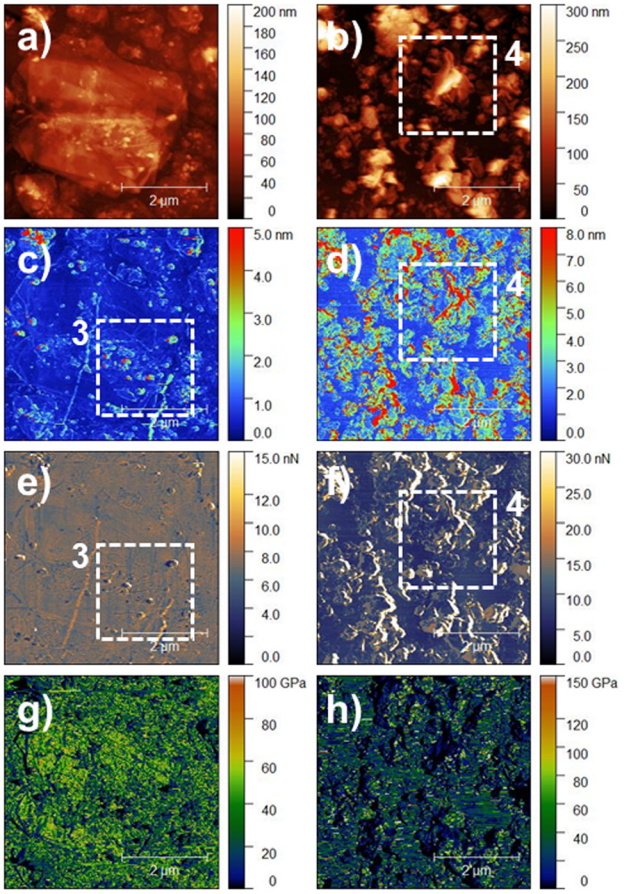

Fig. 8 (a and b) AFM topographic images, (c and d) deformation images, (e and f) adhesion force images and (g and h) Young's modulus images of (a, c, e and g) GO/MoS_2 and (b, d, f and h) rGO/MoS_2 films deposited on an Si/SiO_2 substrate. Topographic, deformation, adhesion force and Young's modulus images were obtained simultaneously and correspond to the same region.

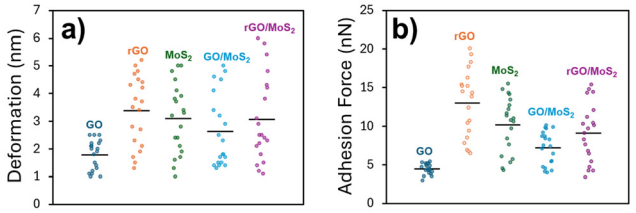

Fig. 9 Scatter plots of (a) deformation and (b) adhesion force that were obtained from 20 points on the GO, rGO, MoS_2, GO/MoS_2 and rGO/MoS_2 films after analyzing the regions in the images.

the integration of GO sheets confers an increased material property. Furthermore, Roy *et al.* demonstrated that modulating the GO-to-MoS_2 ratio generates materials with varying Young's modulus values, where the increased MoS_2 content inversely impacts the stiffness of the material.[58] On the other hand, in the images of the rGO/MoS_2 film, greater deformations and adhesions in the folds of the sheets are noted (dashed square area 4 in Fig. 8). However, the adhesion strength showed a decrease over the length of the film. The Young's modulus value of the film was 25 GPa, showing that the union of the rGO and MoS_2 sheets resulted in an increase in the stiffness of the material. This increase in stiffness in relation to the individual constituents is corroborated by the literature, which suggested that the insertion of graphene sheets between MoS_2 can lead to a three-fold increase in Young's modulus.[59]

The PeakForce-QNM® mode captures images of the adhesion force, deformation, and Young's modulus by recording comprehensive force curves across the entire extent of the analyzed area (more information about the force curves is provided in the ESI, Fig. S6†). Fig. 9 shows the scatter plot of the analyzed areas in the films, which reveals the frequency of occurrence of the respective properties in the materials. Furthermore, Table 1 summarizes all data acquired by PeakForce and compares the stiffness values found in this work with those found in the literature. As observed in the PeakForce images, the rGO film presented the greatest adhesion strength (12.9 nN) and deformation (3.4 nm), which resulted in lower stiffness. On the other hand, the GO film, even though it has intercalated water (which increases adhesion and deformation of the region), has weakly adhered sheets (4.5 nN), which may be linked to the sheets having a stronger interaction with the substrate, and with low deformation (1.8 nm), resulting in the stiffest film observed in this work. In the nanocomposites, a large difference in properties is noted, which is due to the specific interaction of MoS_2 with GO and rGO. The GO/MoS_2 film showed greater deformation (2.6 nm) and adhesion (7.2 nN) when compared to the pure GO film, which resulted in a decrease in stiffness. On the other hand, the rGO/MoS_2 film showed a decrease in its deformation (3.1 nm), in addition to its adhesion strength dropping drastically (9.1 nN), which led to an increase in Young's modulus.

It should be noted that the films analyzed in this manuscript were prepared through a novel methodology, and it is not possible to find similar structures in the literature to compare with the results presented here. Additionally, while prior reports describe properties of single flakes with monolayer thicknesses (~1 nm), the films examined here are approximately 20 nm thick and constituted by the interaction between different flakes. This marked disparity in thickness and assembly suggests that the influence of interaction, func-

Table 1 Mechanical properties of the films compared to the values found in the literature

Film	Deformation (nm)	Adhesion force (nN)	Young's modulus, this work (GPa)	Young's modulus, literature (GPa)
GO	1.8	4.5	78	15–665[41,60,61]
rGO	3.4	12.9	15	5–300[62–65]
MoS_2	3.1	10.2	18	130–330[66–69]
GO/MoS_2	2.6	7.2	30	3–13[58]
rGO/MoS_2	3.1	9.1	25	556[59]

tional groups and structural defects on the properties of the materials is more significant than the influence of the sample/substrate interaction.

4. Conclusion

The results presented here have demonstrated that the combination of different SPM modes allows useful information regarding heterogeneities, interactions, distribution, morphology, topography and structure of components in thin-film nanocomposites to be obtained, enabling the establishment of a clear structure/property relationship. The effect of the substrate and the particle/particle interaction to generate these films was important in order to clarify some results, either by analyzing the same material directly as a thin and continuous film or as small entities resulting from film fragmentation. Also, the specific interaction of one component (MoS_2) with two graphene-like compounds (GO and rGO) was understood and correlated with some properties of the final material. It was demonstrated that the GO-dispersed film exhibits flakes with higher friction than the substrate, while the rGO-dispersed film exhibits lower friction compared to the same substrate. This is due to the number of oxygenated functional groups present in GO that impede the movement of the probe through the sheet. In contrast, the friction among the small flakes of the MoS_2-dispersed film varies due to charge and size distribution. The control films, which are homogeneous and continuous, exhibited spots with more friction, more adhesion and greater deformation correlating with edges and folds of the sheets that are the result of the flake–flake interaction characteristics of the thin-film morphology. Consequently, rGO and MoS_2 films show higher adhesion and deformation, and lower stiffness than the GO film. In the nanocomposites, the GO/MoS_2 film exhibits a large agglomeration of MoS_2 distributed throughout the GO sheets, suggesting a lower interaction between the two materials. In contrast, the rGO/MoS_2 film shows a uniform distribution of small MoS_2 flakes throughout rGO sheets, leading to a significant reduction in the work function when compared to the other nanocomposite materials. Even so, the GO/MoS_2 film shows lower adhesion and deformation than the rGO/MoS_2 film. Nevertheless, when we compared all the analyzed films, the rGO/MoS_2 film had improved nanomechanical properties when compared to the neat rGO film. On the other hand, the nanomechanical properties of GO/MoS_2, when compared with the pure GO film, were compromised due to there being less intimate interaction between the components.

Finally, this work demonstrates the huge versatility and completeness of combining different SPM techniques in the characterization of thin and continuous single- or bi-component films, clarifying important aspects related to the interaction between the components and, consequently, to the resulting synergistic properties, which is crucial for the application of these materials.

Author contributions

The manuscript was written through the contributions of all authors. All authors have given approval to the final version of the manuscript.

Data availability

The data supporting the findings of this study are available within the article and its ESI.†

Conflicts of interest

There are no conflicts to declare.

Acknowledgements

The authors acknowledge the financial support of CNPq, CAPES, FAPEMIG, INCT-Nanocarbono and INCT-NanoVida. Amanda F. Pereira thanks CNPq for the fellowship. Ariane Schmidt thanks CAPES for the fellowship.

References

1 J. Zhang, J. Hu, X. Li, L. Yang, L. Yang, J. Lin, J. Huang and G. Xu, *Chem. Eng. J.*, 2023, **456**, 140972.
2 J. Cai, X. Chen, X. Duan, G. Yang, Q. Zhang, H. Fan, Z. Liu and F. Peng, *Electrochim. Acta*, 2023, **462**, 142705.
3 S. Li, H. Yuan, C. Ye, Y. Wang, L. Wang, K. Ni and Y. Zhu, *J. Mater. Chem. A*, 2023, **11**, 9816–9823.
4 X. Wu, H. Cheng and X. Luo, *Mater. Today Commun.*, 2023, **34**, 105313.
5 S. Gupta, P. Pimenidou, M. Garcia, S. Das and N. Dimakis, *Appl. Surf. Sci.*, 2023, **623**, 156948.
6 F. Giannazzo, S. E. Panasci, E. Schilirò, A. Koos and B. Pécz, *Mater. Sci. Semicond. Process.*, 2024, **174**, 108220.
7 P. Li, H. Guo, R. Duan, G. Ru and W. Qi, *ACS Appl. Electron. Mater.*, 2023, **5**, 1676–1687.
8 Y. Li, Y. Zhang, Y. Wang, J. Sun, Q. You, M. Zhu, L. Li and T. Deng, *Adv. Funct. Mater.*, 2024, **34**, 2302288.
9 D. S. Rana, R. Sharma, S. Kumar, N. Gupta, S. Thakur, K. K. Thakur and D. Singh, *Nano-Struct. Nano-Objects*, 2023, **36**, 101041.
10 F. Khan, C. M. Julien and S. S. Islam, *FlatChem*, 2024, **43**, 100586.
11 E. Enebral-Romero, L. Gutiérrez-Gálvez, R. Del Caño, M. V. Sulleiro, A. Naranjo, I. J. Gómez, F. Pariente, E. M. Pérez, T. García-Mendiola and E. Lorenzo, *Sens. Actuators, B*, 2023, **392**, 134105.
12 Z. Yang, J. Zhu, X. Xu, L. Wang, G. Zhou, Z. Yang and Y. Zhang, *RSC Adv.*, 2023, **13**, 4056–4064.

13 F. Fioravanti, S. Martínez, S. Delgado, G. García, J. L. Rodriguez, E. P. Tejera and G. I. Lacconi, *Electrochim. Acta*, 2023, **441**, 141781.
14 P. Shen, P. Yin, Y. Zou, M. Li, N. Zhang, D. Tan, H. Zhao, Q. Li, R. Yang, B. Zou and B. Liu, *Adv. Mater.*, 2023, **35**, 2212172.
15 Y. Liu, Y. Zhao, L. Jiao and J. Chen, *J. Mater. Chem. A*, 2014, **2**, 13109–13115.
16 Y. Li, H. Wang, L. Xie, Y. Liang, G. Hong and H. Dai, *J. Am. Chem. Soc.*, 2011, **133**, 7296–7299.
17 D. Pandey, R. Reifenberger and R. Piner, *Surf. Sci.*, 2008, **602**, 1607–1613.
18 A. Deshpande and B. J. Leroy, *Phys. E*, 2012, **44**, 743–759.
19 K. Bian, C. Gerber, A. J. Heinrich, D. J. Müller, S. Scheuring and Y. Jiang, *Nat. Rev. Methods Primers*, 2021, **1**, 1–29.
20 F. Lavini, F. Cellini, M. Rejhon, J. Kunc, C. Berger, W. de Heer and E. Riedo, *JPhys Mater.*, 2020, **3**, 024005.
21 S. Luo, T. Alkhidir, S. Mohamed, S. Anwer, B. Li, J. Fu, K. Liao and V. Chan, *Appl. Surf. Sci.*, 2023, **609**, 155303.
22 H. Kim, D. H. Kim, Y. Jeong, D. S. Lee, J. Son and S. An, *Nanoscale Adv.*, 2023, **5**, 2271–2279.
23 A. C. De Palma, X. Peng, S. Arash, F. Y. Gao, E. Baldini, X. Li and E. T. Yu, *Nano Lett.*, 2024, **24**, 1835–1842.
24 X. Tang, Z. Zhang, K. Zheng, Y. Wu, Z. Chen, C. Wang and Z. Shi, *Polymer*, 2023, **281**, 126092.
25 N. Murugesan, S. Suresh, M. Kandasamy, S. Murugesan, N. Pugazhenthiran, V. P. Venkatesh, B. K. Balachandar, S. K. Kumar and M. N. M. Ansari, *Phys. B*, 2023, **669**, 415288.
26 M. Bahri, S. H. Gebre, M. A. Elaguech, F. T. Dajan, M. G. Sendeku, C. Tlili and D. Wang, *Coord. Chem. Rev.*, 2023, **475**, 214910.
27 A. J. G. Zarbin, *Mater. Horiz.*, 2021, **8**, 1409–1432.
28 A. Schmidt, A. F. Pereira and A. J. G. Zarbin, *Chem. – Asian J.*, 2025, **20**, e202401036.
29 W. S. Hummers and R. E. Offeman, *J. Am. Chem. Soc.*, 1958, **80**, 1339.
30 H. Mehl, C. F. Matos, E. G. C. Neiva, S. H. Domingues and A. J. G. Zarbin, *Quim. Nova*, 2014, **37**, 1639–1645.
31 A. Schmidt and A. J. G. Zarbin, *J. Colloid Interface Sci.*, 2019, **554**, 80–90.
32 V. H. R. Souza, S. Husmann, E. G. C. Neiva, F. S. Lisboa, L. C. Lopes, R. V. Salvatierra and A. J. G. Zarbin, *Electrochim. Acta*, 2016, **197**, 200–209.
33 J. E. Sader, J. W. M. Chon and P. Mulvaney, *Rev. Sci. Instrum.*, 1999, **70**, 3967–3969.
34 E. S. Orth, J. G. L. Ferreira, J. E. S. Fonsaca, S. F. Blaskievicz, S. H. Domingues, A. Dasgupta, M. Terrones and A. J. G. Zarbin, *J. Colloid Interface Sci.*, 2016, **467**, 239–244.
35 M. Vishwakarma, D. Varandani, C. Andres, Y. E. Romanyuk, S. G. Haass, A. N. Tiwari and B. R. Mehta, *Sol. Energy Mater. Sol. Cells*, 2018, **183**, 34–40.
36 S. H. Choi, Z. Shaolin and W. Yang, *J. Korean Phys. Soc.*, 2014, **64**, 1550–1555.
37 L. Sygellou, G. Paterakis, C. Galiotis and D. Tasis, *J. Phys. Chem. C*, 2016, **120**, 281–290.
38 C. W. Lee, B. J. Min, S. I. Kim and H. K. Jeong, *Carbon*, 2013, **54**, 353–358.
39 S. Naghdi, G. Sanchez-Arriaga and K. Y. Rhee, *J. Alloys Compd.*, 2019, **805**, 1117–1134.
40 A. Jawaid, D. Nepal, K. Park, M. Jespersen, A. Qualley, P. Mirau, L. F. Drummy and R. A. Vaia, *Chem. Mater.*, 2016, **28**, 337–348.
41 H. Li, K. Yu, C. Li, Z. Tang, B. Guo, X. Lei, H. Fu and Z. Zhu, *Sci. Rep.*, 2015, **5**, 18730.
42 M. Guo, Y. Yang, Y. Leng, L. Wang, H. Dong, H. Liu and W. Li, *J. Mater. Chem. C*, 2017, **5**, 4845–4851.
43 J. Zhang, X. Gao, Q. Xu, T. Ma, Y. Hu and J. Luo, *Appl. Surf. Sci.*, 2021, **546**, 149130.
44 D. Berman, A. Erdemir, A. V. Zinovev and A. V. Sumant, *Diamond Relat. Mater.*, 2015, **54**, 91–96.
45 L. Sun, Z. Wu and R. Niu, *Chem. Phys. Lett.*, 2023, **826**, 140639.
46 H. Ma and R. Bennewitz, *Tribol. Int.*, 2021, **158**, 106925.
47 C. Lee, Q. Li, W. Kalb, X. Z. Liu, H. Berger, R. W. Carpick and J. Hone, *Science*, 2010, **328**, 76–80.
48 E. Yazici, S. Yanik and M. B. Yilmaz, *Carbon*, 2017, **111**, 822–827.
49 J. S. Kim, J. S. Choi, M. J. Lee, B. H. Park, D. Bukhvalov, Y. W. Son, D. Yoon, H. Cheong, J. N. Yun, Y. Jung, J. Y. Park and M. Salmeron, *Sci. Rep.*, 2013, **3**, 2309.
50 M. Paliy, O. M. Braun and S. Consta, *Tribol. Lett.*, 2006, **23**, 7–14.
51 M. R. Vazirisereshk, H. Ye, Z. Ye, A. Otero-De-La-Roza, M. Q. Zhao, Z. Gao, A. T. C. Johnson, E. R. Johnson, R. W. Carpick and A. Martini, *Nano Lett.*, 2019, **19**, 5496–5505.
52 B. Derjaguin, V. Muller and Y. Toporov, *J. Colloid. Interface Sci.*, 1975, **53**, 314–326.
53 N. V. Medhekar, A. Ramasubramaniam, R. S. Ruoff and V. B. Shenoy, *ACS Nano*, 2010, **4**, 2300–2306.
54 S. Li, X. Chen, F. Liu, Y. Chen, B. Liu, W. Deng, B. An, F. Chu, G. Zhang, S. Li, X. Li and Y. Zhang, *ACS Appl. Mater. Interfaces*, 2019, **11**, 11636–11644.
55 E. Lee, S. G. Lee, W. H. Lee, H. C. Lee, N. N. Nguyen, M. S. Yoo and K. Cho, *Chem. Mater.*, 2020, **32**, 4544–4552.
56 E. Pollmann, S. Sleziona, T. Foller, U. Hagemann, C. Gorynski, O. Petri, L. Madauß, L. Breuer and M. Schleberger, *ACS Omega*, 2021, **6**, 15929–15939.
57 S. E. Panasci, E. Schilirò, G. Greco, M. Cannas, F. M. Gelardi, S. Agnello, F. Roccaforte and F. Giannazzo, *ACS Appl. Mater. Interfaces*, 2021, **13**, 31248–31259.
58 A. K. Roy, S. N. Faisal, A. Spickenheuer, C. Scheffler, J. Wang, A. T. Harris, A. I. Minett and M. S. Islam, *Carbon Trends*, 2021, **5**, 100097.
59 J. W. Jiang and H. S. Park, *Appl. Phys. Lett.*, 2014, **105**, 3–8.
60 J. W. Suk, R. D. Piner, J. An and R. S. Ruoff, *ACS Nano*, 2010, **4**, 6557–6564.
61 K. Adstedt, M. L. Buxton, L. C. Henderson, D. J. Hayne, D. Nepal, Y. Gogotsi and V. V. Tsukruk, *Carbon*, 2023, **203**, 161–171.

62 M. C. F. Costa, P. R. Ng, S. Grebenchuck, J. Y. Tan, G. K. W. Koon, H. L. Tan, C. R. Woods, R. K. Donato, K. S. Novoselov and A. H. Castro Neto, *Carbon*, 2023, **208**, 140–147.
63 C. Gómez-Navarro, M. Burghard and K. Kern, *Nano Lett.*, 2008, **8**, 2045–2049.
64 A. Nekahi, P. H. Marashi and D. Haghshenas, *Appl. Surf. Sci.*, 2014, **295**, 59–65.
65 Y. Zhang and C. Pan, *Diamond Relat. Mater.*, 2012, **24**, 1–5.
66 N. Ghobadi, *Curr. Appl. Phys.*, 2017, **17**, 1483–1493.
67 S. Bertolazzi, J. Brivio and A. Kis, *ACS Nano*, 2011, **5**, 9703–9709.
68 D. Gupta, V. Chauhan and R. Kumar, *Inorg. Chem. Commun.*, 2020, **121**, 108200.
69 M. Ramos, J. Nogan, M. Ortíz-Díaz, J. L. Enriquez-Carrejo, C. A. Rodriguez-González, J. Mireles-Jr-Garcia, C. Ornelas and A. Hurtado-Macias, *Surf. Topogr.:Metrol. Prop.*, 2017, **5**, 025003.